

Multidimensional Purcell effect in an ytterbium-doped ring resonator

Dapeng Ding¹, Lino M. C. Pereira², Jared F. Bauters³, Martijn J. R. Heck³, Gesa Welker¹, André Vantomme², John E. Bowers³, Michiel J. A. de Dood¹ and Dirk Bouwmeester^{1,4*}

Rare-earth ions in solids are of particular interest for quantum information storage and processing because of the long coherence times of the 4f states¹. In the past few years, substantial progress has been made by using ensembles of ions^{2–6} and single ions^{7–10}. However, the weak optical transitions within the 4f manifold pose a great challenge to the optical interaction with a single rare-earth ion on a single-photon level. Here, we demonstrate a ninefold enhanced ion–light interaction (Purcell effect¹¹) in an integrated-optics-based, fibre-coupled silicon nitride (Si₃N₄) ring resonator with implanted ytterbium ions (Yb³⁺). We unveil the one-, two- and three-dimensional contributions to the Purcell factor as well as the temperature-dependent decoherence and depolarization of the ions. The results indicate that this cavity quantum electrodynamics (QED) system has the potential of interfacing single rare-earth ions with single photons on a chip.

Due to the dipole-forbidden nature of the 4f–4f transitions of rare-earth ions, their oscillator strengths are very small ($\sim 1 \times 10^{-6}$). To overcome this limitation, a high-quality-factor (Q) and small-mode-volume (V) (high Q/V) optical cavity can be used to enhance the ion–light interaction in the framework of cavity quantum electrodynamics (QED). In the weak coupling regime of cavity QED, this effect is characterized by the Purcell factor, which quantifies the enhancement of the spontaneous emission (SE) rate. To date, the SE of rare-earth ions has been studied in photonic-crystal cavities^{12–14}, whispering-gallery mode ring resonators¹⁵ and Fabry–Perot cavities^{16–18}. An erbium-doped Si₃N₄ ring resonator was also studied in ref. 12, but no cavity QED phenomena were observed due to the low Q/V of the particular ring resonator.

In this Letter, we investigate an Yb³⁺-doped high-Q ($\sim 5 \times 10^6$) Si₃N₄ ring resonator that has an advantage over other types of microcavity because of its all-integrated-optics approach. Because of the structure of the ring resonator, not only is the cavity Purcell effect present, but enhancements from waveguide modes also exist. The former effect is spectrally narrowband and becomes appreciable only in the vicinity of the cavity resonance, while the latter effect is intrinsically broadband^{19,20}. The long excited-state lifetime of the 4f–4f transition makes thermal depolarization of Yb³⁺ dipoles important²¹. This causes the coupling of the ions to the modes in all polarizations, even though the ions are initially resonantly excited in a well-defined polarization.

Here, we introduce a model that separates the different contributions to the SE rate into three discrete channels: a one-dimensional (1D) enhancement from the slab waveguide, a two-dimensional (2D) enhancement from the channel waveguide and the three-dimensional (3D) Purcell effect from the cavity²². We refer to these effects as 1D, 2D and 3D Purcell effects. Measurements of the total Purcell factor, depolarization and

decoherence as functions of temperature shed light on the different contributions to the enhanced SE rate.

The ring resonator (radius of 1.59 mm) consists of a Si₃N₄ core embedded in amorphous SiO₂ cladding^{23–26}. A schematic, photograph and cross-section of the ring resonator are presented in Fig. 1a–c. The Si₃N₄ core has a width of 2.8 μm and a thickness of 0.1 μm . Yb ions are implanted into the device with a peak concentration of $\sim 0.001\%$ (atom numbers). The ions are laterally uniform and are approximately Gaussian distributed in depth with a full-width at half-maximum of 86 nm and a centre 72 nm above the Si₃N₄ top surface (see Methods). The ring resonator is coupled to two waveguides. A single-mode fibre and three multimode fibres are coupled to the waveguides (see Methods).

An energy level diagram of Yb³⁺ in SiO₂ is presented in Fig. 2a. We focus on the optical transition centred at 976 nm, which involves the lowest manifold of the ground state (²F_{7/2}) and the lowest manifold of the excited state (²F_{5/2}) (see Supplementary Fig. 4 for emission spectra). Energy transfer among adjacent ions is the dominant non-radiative decay mechanism for Yb³⁺ (ref. 27), as illustrated in Fig. 2b. Around 976 nm, the ring resonator supports two transverse magnetic (TM) modes and three transverse electric (TE) modes (Supplementary Fig. 2). Profiles of the fundamental modes denoted by ‘TM₀’ and ‘TE₀’ are shown in Fig. 1d,e, which correspond to the 2D waveguide modes and cross-sections of the 3D ring resonator modes. The 1D modes are calculated for an infinite Si₃N₄ slab sandwiched in SiO₂ cladding, resulting in two 1D modes, the profiles of which are shown in Fig. 1f,g. The electric fields of the TM (TE) modes are approximately linearly polarized along the y (x) direction. The measured values of Q at 976.0 nm are 4.8×10^6 and 8.3×10^5 for the 3D TM₀ and TE₀ modes, respectively (Supplementary Fig. 3).

A schematic of the set-up used to measure the SE decay rate of Yb³⁺ is shown in Fig. 2c. The device was mounted in a closed-cycle dilution refrigerator. The output of a narrow-linewidth (~ 100 kHz) laser at 976.0 nm was modulated by a mechanical chopper and coupled to fibre 1 through a fibre polarization controller (FPC). The resulting laser pulse has an ‘on’ (‘off’) time of 1 (9) ns and a measured rise and fall time of less than 0.5 μs . The laser frequency was locked to the 3D TM₀ mode (see Methods). The FPC was set to maximize the transmission at fibre 2. SE events of the Yb³⁺ ensemble were counted at the output of fibre 4 with time bins of 0.5 μs through a bandpass filter ($\lambda_0 = 976$ nm, $\Delta\lambda = 2$ nm).

Three SE decay traces measured at 295 K, 5.7 K and 50 mK are shown in Fig. 3. These are not single-exponential functions because of the spatial and spectral distributions of Yb³⁺ and therefore the variations in the Purcell factors. The fastest decay rate for the trace at 50 mK is clearly greater than those at 295 and 5.7 K. We are interested in the maximum Purcell factor F_m , which is

¹Huygens-Kamerlingh Onnes Laboratory, Leiden University, Leiden, 2333 CA, Netherlands. ²KU Leuven, Instituut voor Kern- en Stralingsfysica, Leuven 3001, Belgium. ³Department of Electrical and Computer Engineering, University of California Santa Barbara, Santa Barbara, California 93106, USA. ⁴Department of Physics, University of California Santa Barbara, Santa Barbara, California 93106, USA. *e-mail: bouwmeester@physics.ucsb.edu

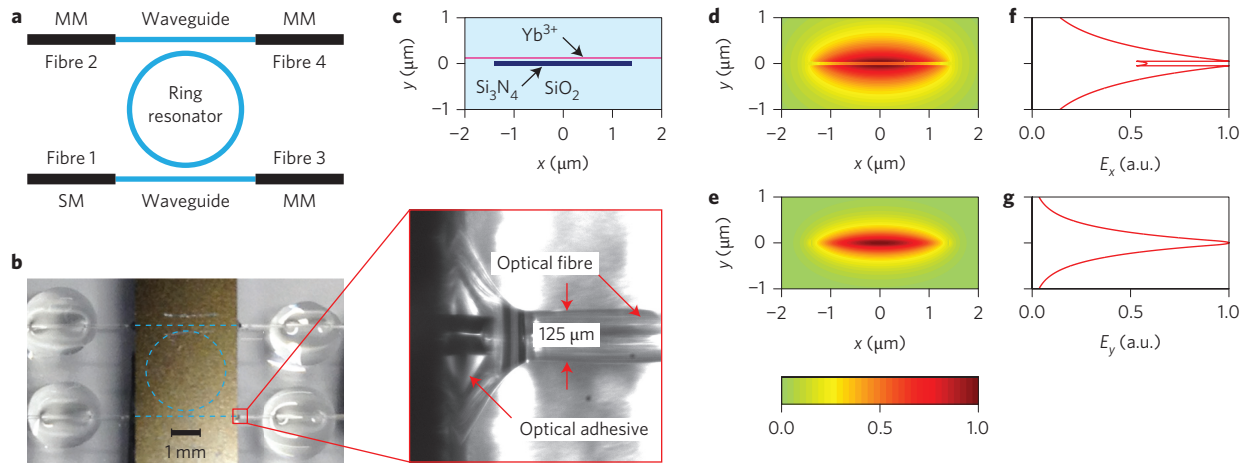


Figure 1 | Fibre-coupled Si_3N_4 ring resonator doped with Yb^{3+} . **a**, Schematic top view of a ring resonator coupled to two straight waveguides and subsequently to four optical fibres. Fibre 1 is single-mode (SM) and fibres 2–4 are multimode (MM). **b**, Photograph of the device and microscopic image of the fibre-waveguide coupling. **c**, Schematic cross-section of the ring resonator consisting of a Si_3N_4 core embedded in SiO_2 cladding with Yb^{3+} implanted above the Si_3N_4 core. **d, e**, Calculated mode profiles of TM_0 (**d**) and TE_0 (**e**) at 976 nm for the waveguide as shown in **c**. The colour plot in **d** (**e**) represents the y (x) component of the electric field, E_y (E_x). **f, g**, Calculated mode profiles of TM_0 (**f**) and TE_0 (**g**) at 976 nm for a slab waveguide with a 0.1- μm -thick Si_3N_4 layer in the x - z plane sandwiched in SiO_2 .

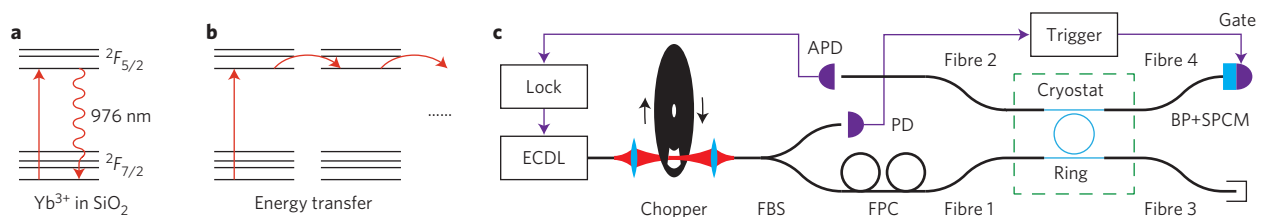


Figure 2 | Energy level diagram of Yb^{3+} and experimental set-up. **a**, Energy level diagram of an Yb^{3+} ion in SiO_2 with relevant transitions indicated by red arrows. **b**, Energy level diagram of two Yb^{3+} ions illustrating the energy transfer between their excited states as non-radiative decay. **c**, Schematic of the set-up used to measure the spontaneous emission (SE) decay rate of Yb^{3+} in a ring resonator. ECDL, external cavity diode laser; FBS, fibre beamsplitter; FPC, fibre polarization controller; Ring, Yb^{3+} -doped ring resonator; PD, photodetector; APD, avalanche photodetector; BP, bandpass filter; SPCM, single-photon-counting module; Lock, frequency modulation locking. Black curves denote optical fibres and purple lines denote electrical wirings.

defined as the net enhancement in addition to the free-space SE decay rate k_0 such that the maximum SE decay rate is given by $k_0 + k_R F_m$, with k_R being a free-space radiative decay rate. To extract F_m from the traces, we constructed a decay function $I(t)$ with $k_0 \equiv k_R + k_{ET}$ and $k_m \equiv k_R F_m$ as two parameters, where k_{ET} is an energy transfer rate among ions (see Methods). From fitting the trace at a given temperature with $I(t)$, we obtained the values of k_0 and k_m . Examples at 295 K, 5.7 K and 50 mK are shown in Fig. 3 with $k_0 = 1.41, 1.30$ and $2.00 (\pm 0.01) \text{ ms}^{-1}$ and $k_m = 1.2, 4.6$ and $11.7 (\pm 0.2) \text{ ms}^{-1}$, respectively. $I(t)$ is in good agreement with the traces at 295 K, 5.7 K and also with the initial 1 ms of the trace at 50 mK, but it apparently deviates from the trace at 50 mK at longer times leading to an artificially large value of k_0 (2.00 ms^{-1}) (see Methods for further discussion). Nevertheless, the extracted value of k_m is always reliable because the fastest decay occurs within the initial 1 ms, to which part of the trace $I(t)$ yields a very good fit (inset of Fig. 3). The fact that at 5.7 K the value of $k_0 + k_m$ is large and the value of k_0 is small compared with those at 295 K causes the crossing of the two traces.

Figure 4a shows the values of k_0 at different temperatures. k_0 decreases with decreasing temperature down to about 10 K due to the decreasing non-radiative decay rate. The model $k_0 = k_R + k_{ET}$ is fitted to the data above 10 K as shown in Fig. 4a, where $k_{ET}(T) = B \exp(-\beta/T)$, as given by ref. 27, with k_R, B and β as parameters. The fit results in $k_R = 1.30 \pm 0.01 \text{ ms}^{-1}$, $B = 0.13 \pm 0.01 \text{ ms}^{-1}$ and $\beta = 51 \pm 7 \text{ K}$.

The measured Purcell factor $F_m = k_m/k_R$ is shown in Fig. 4b (and inset). F_m is approximately constant at high temperature with a value of ~ 0.8 and increases rapidly when $T < 50 \text{ K}$, reaching a value of 9.0 at 50 mK. To interpret the results, we introduce a model that includes multidimensional Purcell effects and dipole depolarization. We neglect the Purcell effects from higher-order modes. F_m can be written as a sum of contributions over all the dimensions and modes²²:

$$F_m = (F_p^1 + F_p^2 + F_p^3) f_p (1 + 2\Theta) / 3 + (2F_q^1 + F_q^2 + F_q^3) f_q (1 - \Theta) / 3 \quad (1)$$

where F^1, F^2 and F^3 are 1D, 2D and 3D Purcell factors for $p \equiv \text{TM}_0$ or $q \equiv \text{TE}_0$ modes, respectively, f_p and f_q account for the reduction of the Purcell factor because the ions are located away from the field maximum and $0 \leq \Theta \leq 1$ quantifies the degree to which the ions maintain their initial dipole directions during the lifetime (see Supplementary Section 1 for details of the model). F^1 and F^2 are independent of temperature, while the expression for F^3 contains the homogeneous linewidth of Yb^{3+} denoted by Γ_H and therefore F^3 is temperature-dependent.

It has been found that $\Gamma_H(T) \propto T^{1.8}$ at high temperature due to the coupling to phonons and $\Gamma_H(T) \propto T^{1.3}$ at low temperature due to coupling to tunnelling systems²⁸. Here we assume that the crossover occurs at 40 K (following ref. 28). We measure $\Gamma_H(T)$ using photon echo techniques (see Methods and Supplementary Section 4), the results of which are shown in Fig. 5a. Below 80 mK,

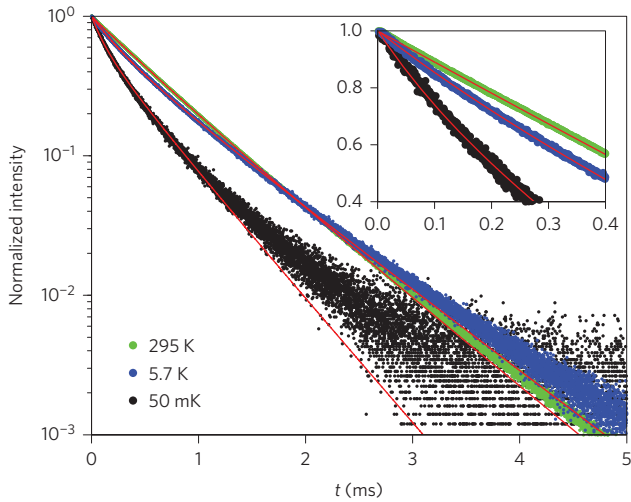


Figure 3 | Spontaneous emission (SE) decay traces. Measured SE decay traces at 295 K (green dots), 5.7 K (blue dots) and 50 mK (black dots) in a log-linear scale with time (t) bins of 0.5 μ s and the fits (red curves) to a decay function. Data were obtained by averaging over 5×10^5 single decay traces. Dark counts are subtracted and maximum counts are normalized to unity. The absolute maximum counts of the data decrease with decreasing temperature, because less ions overlap spectrally with the excitation laser. Inset: magnification of the main graph in the initial 0.4 ms.

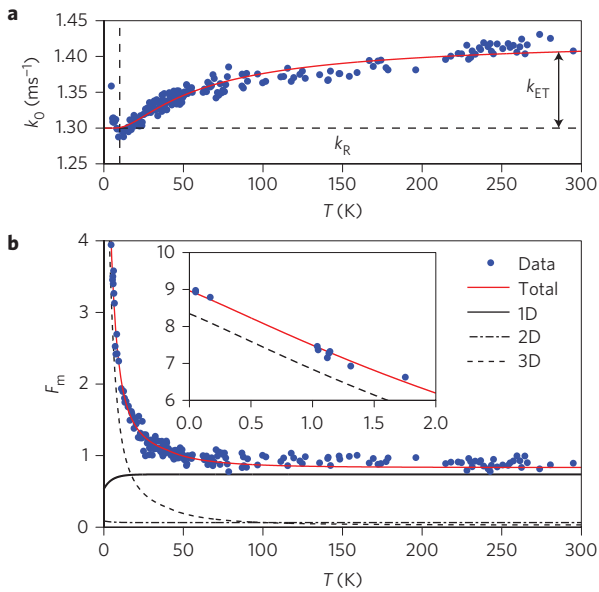


Figure 4 | Free-space decay rate and maximum Purcell factor. **a**, Measured free-space decay rate k_0 (blue dots) and fit (red curve) using the model assuming a constant radiative decay rate k_R (horizontal line) and a temperature-dependent energy transfer rate k_{ET} . Below 10 K (vertical line), k_0 increases to 2.00 ms^{-1} (out of scale) at 50 mK with decreasing temperature (T) as an artefact of the decay function. Only the data above 10 K are used for the fit. **b**, Measured maximum Purcell factor F_m (blue dots) and fit (red curve) using the model based on the multidimensional Purcell effects and dipole depolarization. The 1D (black solid), 2D (black dashed-dotted) and 3D (black dashed) components are also shown. Inset: same physical quantities as in **b**, below 2 K.

$\Gamma_H(T)$ depends weakly on temperature, as reported previously in ref. 29. For 80 mK $< T < 150$ mK, $\Gamma_H(T)$ is well described by a power law of $T^{1.3}$ with $\Gamma_H(1\text{K}) = 2.1 \pm 0.1$ MHz. We also measure Θ using polarization analysis of the resonance fluorescence (see

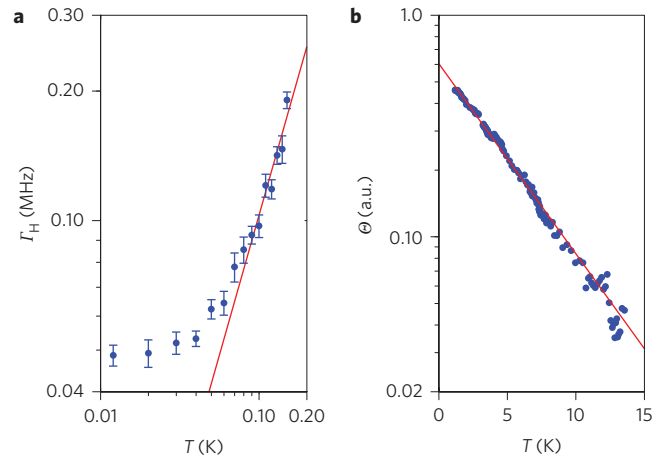


Figure 5 | Homogeneous linewidth and dipole polarization.

a, Homogeneous linewidth $\Gamma_H(T)$ obtained using the two-pulse photon echo technique (blue dots) and fit to data above 80 mK using a function of $\Gamma_H(1\text{K}) \times T^{-1.3}$ (red line) with $\Gamma_H(1\text{K}) = 2.1 \pm 0.1$ MHz. Error bars indicate 95% confidence intervals (two standard deviations). **b**, Dipole polarization Θ obtained by analysing the polarization of the resonance fluorescence (blue dots) and fit using an exponential function as $\exp(-T/\alpha)$ with $\alpha = 5.1 \pm 0.1$ K (red line).

Methods and Supplementary Section 5) and show the results in Fig. 5b. Θ decreases exponentially as a function of temperature with parameter $\alpha = 5.1 \pm 0.1$ K. Because photon echo and lifetime experiments are performed on largely different timescales (microsecond versus millisecond), spectral diffusion has a larger impact on the lifetime measurements, leading to a larger value of $\Gamma_H(T)$ (ref. 30). To accommodate this, $\Gamma_H(1\text{K})$ is treated as the only adjustable parameter in the model. All the other parameters are either obtained through numerical simulations or extracted from measurements.

The fit of equation (1) to the data is shown in Fig. 4b (and inset), resulting in $\Gamma_H(1\text{K}) = 4.8 \pm 0.2$ MHz. As expected, this value is larger than that measured with photon echo experiments by a factor of 2.3 due to spectral diffusion. Contributions from the 1D, 2D and 3D Purcell effects are shown separately in the figure. The 1D and 2D Purcell factors are constants at the high temperature limit with $\Theta \approx 0$, but they approach the values for TM_0 when $T \ll \alpha$ ($\Theta \approx 1$). The 3D Purcell factor is relatively small at high temperature, but it becomes appreciable for $T < 50$ K where $\Gamma_H(T)$ is comparable to or smaller than the linewidth of the 3D TM_0 mode (64 MHz). Ultimately, the value of F_m reaches 9.0 at 50 mK, where the 3D Purcell effect is dominant and is almost entirely determined by the large Q/V of the 3D TM_0 mode. Our unique approach of cavity QED has the potential to increase this number through further optimization of the design of the ring resonator. Because of the broadband nature of the 1D and 2D Purcell effects, their temperature dependences are very weak compared to the 3D Purcell effect. This study is therefore best suited to demonstrating the most important 3D Purcell effect and separating it from the combined 1D and 2D effects.

In conclusion, we have introduced a novel solid-state cavity QED system based on high- Q Si_3N_4 ring resonators with implanted rare-earth ions. We have separated the 3D contribution to the Purcell effect from the 1D and 2D contributions and have analysed the temperature dependence. This provides novel insight into the temperature dependence of the decoherence and depolarization of the rare-earth ions. The results indicate that the system has the potential of interfacing single rare-earth ions with single photons on a chip.

Methods

Methods and any associated references are available in the [online version of the paper](#).

Received 18 May 2015; accepted 16 March 2016;
published online 25 April 2016

References

- Fraval, E., Sellars, M. J. & Longdell, J. J. Dynamic decoherence control of a solid-state nuclear-quadrupole qubit. *Phys. Rev. Lett.* **95**, 030506 (2005).
- Clausen, C. *et al.* Quantum storage of photonic entanglement in a crystal. *Nature* **469**, 508–511 (2011).
- Saglamyurek, E. *et al.* Broadband waveguide quantum memory for entangled photons. *Nature* **469**, 512–515 (2011).
- Usmani, I. *et al.* Heralded quantum entanglement between two crystals. *Nature Photon.* **6**, 234–237 (2012).
- Saglamyurek, E. *et al.* Quantum storage of entangled telecom-wavelength photons in an erbium-doped optical fibre. *Nature Photon.* **9**, 83–87 (2015).
- Zhong, M. *et al.* Optically addressable nuclear spins in a solid with a six-hour coherence time. *Nature* **517**, 177–180 (2015).
- Kolesov, R. *et al.* Optical detection of a single rare-earth ion in a crystal. *Nature Commun.* **3**, 1029 (2012).
- Siyushev, P. *et al.* Coherent properties of single rare-earth spin qubits. *Nature Commun.* **5**, 3895 (2014).
- Yin, C. *et al.* Optical addressing of an individual erbium ion in silicon. *Nature* **497**, 91–94 (2013).
- Utikal, T. *et al.* Spectroscopic detection and state preparation of a single praseodymium ion in a crystal. *Nature Commun.* **5**, 3627 (2014).
- Purcell, E. M. Spontaneous emission probabilities at radio frequencies. *Phys. Rev.* **69**, 681 (1946).
- Gong, Y. *et al.* Linewidth narrowing and Purcell enhancement in photonic crystal cavities on an Er-doped silicon nitride platform. *Opt. Express* **18**, 2601–2612 (2010).
- Gong, Y. *et al.* Observation of transparency of erbium-doped silicon nitride in photonic crystal nanobeam cavities. *Opt. Express* **18**, 13863–13873 (2010).
- Zhong, T., Kindem, J. M., Miyazono, E. & Faraon, A. Nanophotonic coherent light-matter interfaces based on rare-earth-doped crystals. *Nature Commun.* **6**, 8206 (2015).
- McAuslan, D. L., Korystov, D. & Longdell, J. J. Coherent spectroscopy of rare-earth-metal-ion-doped whispering-gallery-mode resonators. *Phys. Rev. A* **83**, 063847 (2011).
- Vredenberg, A. M. *et al.* Controlled atomic spontaneous emission from Er^{3+} in a transparent Si/SiO₂ microcavity. *Phys. Rev. Lett.* **71**, 517–520 (1993).
- Lipson, M. & Kimerling, L. C. Er^{3+} in strong light-confining microcavity. *Appl. Phys. Lett.* **77**, 1150–1152 (2000).
- Goto, H., Nakamura, S., Kujiraoka, M. & Ichimura, K. Cavity-enhanced spectroscopy of a rare-earth-ion-doped crystal: observation of a power law for inhomogeneous broadening. *Opt. Express* **21**, 24332–24343 (2013).
- Urbach, H. P. & Rikken, G. L. J. A. Spontaneous emission from a dielectric slab. *Phys. Rev. A* **57**, 3913–3930 (1998).
- Jun, Y. C., Briggs, R. M., Atwater, H. A. & Brongersma, M. L. Broadband enhancement of light emission in silicon slot waveguides. *Opt. Express* **17**, 7479–7490 (2009).
- Jamison, S. P. & Reeves, R. J. Optical depolarization in $\text{CaF}_2\text{:RE}^{3+}$ and $\text{SrF}_2\text{:RE}^{3+}$ C_{4v} centers due to dipole reorientation. *J. Lumin.* **66–67**, 169–173 (1995).
- Genov, D. A., Oulton, R. F., Bartal, G. & Zhang, X. Anomalous spectral scaling of light emission rates in low-dimensional metallic nanostructures. *Phys. Rev. B* **83**, 245312 (2011).
- Bauters, J. F. *et al.* Ultra-low-loss high-aspect-ratio Si₃N₄ waveguides. *Opt. Express* **19**, 3163–3174 (2011).
- Tien, M.-C. *et al.* Ultra-high quality factor planar Si₃N₄ ring resonators on Si substrates. *Opt. Express* **19**, 13551–13556 (2011).
- Bauters, J. F. *et al.* Planar waveguides with less than 0.1 dB/m propagation loss fabricated with wafer bonding. *Opt. Express* **19**, 24090–24101 (2011).
- Ding, D. *et al.* Fano resonances in a multimode waveguide coupled to a high-Q silicon nitride ring resonator. *Opt. Express* **22**, 6778–6790 (2014).
- Yeh, D. C., Sibley, W. A., Suscavage, M. & Drexhage, M. G. Radiation effects and optical transitions in Yb³⁺-doped barium-thorium fluoride glass. *J. Non-Cryst. Solids* **88**, 66–82 (1986).
- Brundage, R. T. & Yen, W. M. Low-temperature homogeneous linewidths of Yb³⁺ in inorganic glasses. *Phys. Rev. B* **33**, 4436–4438 (1986).
- Hegarty, J., Broer, M. M., Golding, B., Simpson, J. R. & MacChesney, J. B. Photon echoes below 1 K in a Nd³⁺-doped glass fiber. *Phys. Rev. Lett.* **51**, 2033–2035 (1983).
- Staudt, M. U. *et al.* Investigations of optical coherence properties in an erbium-doped silicate fiber for quantum state storage. *Opt. Commun.* **266**, 720–726 (2006).

Acknowledgements

The authors thank M.P. van Exter for scientific discussions and proofreading of the manuscript, and A.M.J. den Haan, J.J.T. Wagenaar, M. de Wit and T.H. Oosterkamp for operating the dilution refrigerator. This work is part of the research programme of the Foundation for Fundamental Research on Matter (FOM), which is part of the Netherlands Organisation for Scientific Research (NWO). This work was supported by NWO VICI grant no. 680-47-604, NSF DMR-0960331, NSF PHY-1206118, DARPA MTO under EPHI contract HR0011-12-C-0006 and the Fund for Scientific Research–Flanders (FWO).

Author contributions

J.F.B., M.J.R.H. and J.E.B. fabricated the ring resonator. L.M.C.P. and A.V. performed the ion implantation. G.W. contributed to the low-temperature measurements. D.D. designed and performed all the measurements and, with M.J.A.D. and D.B., analysed the data and wrote the manuscript.

Additional information

Supplementary information is available in the [online version of the paper](#). Reprints and permissions information is available online at www.nature.com/reprints. Correspondence and requests for materials should be addressed to D.B.

Competing financial interests

The authors declare no competing financial interests.

Methods

Ion implantation. Yb³⁺ ions were introduced into the device using ion implantation techniques. Yb²⁺ ions in the implanter were first selected to have only the isotope ¹⁷⁴Yb with zero nuclear spin, and were then implanted with an energy of 360 keV perpendicular to the device with a 200-nm-thick top cladding. After implantation, Rutherford backscattering spectrometry was performed on a reference sample and the data were analysed using NDF³¹ (Supplementary Fig. 1). The implantation energy was chosen carefully so as not to introduce Yb ions into the Si₃N₄ core, because elimination of implantation defects in SiO₂ and Si₃N₄ requires different annealing temperatures and their temperature ranges are incompatible with each other³². The device was completed by wafer bonding at 950 °C for 3 h, which also anneals implantation defects in SiO₂.

Fibre connections. The fibre connections to the waveguides were permanent and compatible with cryogenic temperature. A stripped and cleaved optical fibre was first dipped into a small droplet (diameter smaller than 0.5 mm, generated at the tip of a syringe needle) of ultraviolet curing optical adhesive (NOA61, Norland Products). Once the fibre was retracted from the adhesive droplet, a tiny amount of ball-shaped adhesive was attached at the fibre tip. The fibre was then aligned with the waveguide by maximizing the measured resonance transmission and was arranged protruding towards the waveguide facet. Once the adhesive on the fibre tip touched the waveguide, surface tension pulled the adhesive to the coupling point and rendered the coupling area well surrounded by the adhesive. Subsequently, the adhesive was cured by ultraviolet light. The small and axisymmetric adhesive spot at the coupling point ensured that negligible misalignment was induced by thermal contraction of the adhesive itself while cooling to cryogenic temperature.

Laser frequency stabilization. The laser frequency was locked to the top of the fringe of the TM₀ mode of the ring resonator during the experiment to compensate for thermal drifts. The laser current was modulated with a small sinusoidal wave at 100 kHz. The signal of the APD was demodulated with a lock-in amplifier to generate an error signal, which was fed back to the laser piezo controller through a proportional-integral controller. The locking was stable, even though the laser light was blocked repetitively by the mechanical chopper.

Decay function. We assumed that the Purcell factor distribution along the Yb³⁺ sheet ($y = y_0$ and $z = 0$, $i = \text{TM}_0$ or TE_0) can be approximated as a Gaussian function $h(x)$ at a specific temperature. The position-dependent decay rate $k(x)$ is then readily available as

$$k(x) = k_R + k_{ET} + h(x)k_R F_m \equiv k_0 + h(x)k_m$$

with $h(0) = 1$. The probability density of Yb³⁺ decaying with rate k is proportional to the number of ions dN in an infinitesimal interval dk around k :

$$P(k) \propto \left| \frac{dN}{dk} \right| = 2\rho \left| \frac{dx}{dk} \right|_{x>0} = 2\rho \left| \frac{dk}{dx} \right|_{x>0}^{-1}$$

where ρ is a linear doping density of Yb³⁺. By using a Gaussian function of $h(x)$, we obtain

$$P(k) = \frac{A/(k - k_0)}{\sqrt{\ln k_m - \ln(k - k_0)}}, \quad k_0 < k < k_0 + k_m$$

and $P(k) = 0$ elsewhere, where A is a normalization factor rendering $\int P(k)dk = 1$. The excited-state population of Yb³⁺ is given by $W/(k + 2W)$ according to the steady-state solution of the rate equations, where W is the excitation rate. A decay function $I(t)$ can be built as

$$I(t) \propto \int \frac{W}{k + 2W} P(k)k \exp(-kt) dk$$

We assume that W is independent of k and is small compared to k . $I(t)$ can be simplified as

$$I(t) = \int P(k)\exp(-kt)dk, \text{ with } I(0) = 1$$

which is used to analyse the measured SE decay traces. W increases with decreasing temperature due to the decreasing homogeneous linewidth of Yb³⁺. At low temperature, the assumption of $W \ll k$ remains valid for large k values, but it becomes invalid for small k values. This explains the deviation of the decay function from the slow components of the decay trace at 50 mK, resulting in an artificially large value of k_0 , whereas the fit is precise for the fast components, resulting in a correct value of k_m .

Photon echo. Two laser pulses with widths of 60 and 120 ns were generated with two acousto-optic modulators in series and coupled to the 3D TM₁ mode of the ring resonator through fibre 1. Photon echo occurred after the second pulse and was measured through fibre 3 using a SPCM. The echo intensity was maximized by adjusting the laser power while keeping the pulse widths constant. After this optimization, the two pulses ideally performed $\pi/2$ and π operations for the ions. The echo intensities were measured with varying delay time between the two pulses at a certain temperature. The data are well fitted with a single-exponential function of delay time. The time constant τ extracted from the fit is related to $\Gamma_H(T)$ as $\Gamma_H(T) = 1/4\pi\tau$ (see Supplementary Section 4 for details).

Dipole depolarization. The laser output was modulated with a mechanical chopper and coupled to the 3D TM₁ mode of the ring resonator through a beamsplitter and fibre 1. The fluorescence of Yb³⁺ was coupled back to fibre 1 and the reflective port of the beamsplitter. The polarization of the resonance fluorescence was analysed using a bandpass filter, wave plates, a polarizing beamsplitter and two SPCMs. The wave plates were adjusted when the ring resonator was cooled to 10 mK with fully polarized dipoles of Yb³⁺ such that the integrated signal of one SPCM denoted C_1 was maximized and the integrated signal of the other SPCM denoted C_2 was simultaneously minimized. Coupling and detection efficiencies were calibrated at room temperature with fully depolarized dipoles. The efficiency factor η is given by $\eta = C_2/C_1$, where C_1 and C_2 are the values of C_1 and C_2 at room temperature. The dipole polarization θ is given by $\theta = (\eta C_1 - C_2)/(\eta C_1 + C_2)$ (see Supplementary Section 5 for details).

References

31. Barradas, N. P., Jeynes, C. & Webb, R. P. Simulated annealing analysis of Rutherford backscattering data. *Appl. Phys. Lett.* **71**, 291–293 (1997).
32. Polman, A., Jacobson, D. C., Eaglesham, D. J., Kistler, R. C. & Poate, J. M. Optical doping of waveguide materials by MeV Er implantation. *J. Appl. Phys.* **70**, 3778–3784 (1991).